The Astronomical Journal, 164:61 (15pp), 2022 August https://doi.org/10.3847/1538-3881/ac77f8

The Galactic Distribution of Phosphorus: A Survey of 163 Disk and Halo Stars[*]

Zachary G. Maas[1,2], Keith Hawkins[2], Natalie R. Hinkel[3], Phillip Cargile[4], Steven Janowiecki[5], and Tyler Nelson[2]
[1] McDonald Observatory, The University of Texas at Austin, 2515 Speedway Boulevard, Austin, TX 78712, USA; zgmaas@utexas.edu
[2] Department of Astronomy, The University of Texas at Austin, 2515 Speedway Boulevard, Austin, TX 78712, USA
[3] Southwest Research Institute, 6220 Culebra Road, San Antonio, TX 78238, USA
[4] Center for Astrophysics | Harvard & Smithsonian, 60 Garden Street, Cambridge, MA 02138, USA
[5] University of Texas, Hobby–Eberly Telescope, McDonald Observatory, TX 79734, USA

Received 2022 April 1; revised 2022 June 3; accepted 2022 June 6; published 2022 July 20

Abstract

Phosphorus (P) is a critical element for life on Earth, yet the cosmic production sites of P are relatively uncertain. To understand how P has evolved in the solar neighborhood, we measured abundances for 163 FGK stars over a range of $-1.09 < [\mathrm{Fe/H}] < 0.47$ using observations from the Habitable-zone Planet Finder instrument on the Hobby–Eberly Telescope. Atmospheric parameters were calculated by fitting a combination of astrometry, photometry, and Fe I line equivalent widths. Phosphorus abundances were measured by matching synthetic spectra to a P I feature at 10529.52 Å. Our [P/Fe] ratios show that chemical evolution models generally underpredict P over the observed metallicity range. Additionally, we find that the [P/Fe] differs by ∼0.1 dex between thin disk and thick disk stars that were identified with kinematics. The P abundances were compared with α-elements, iron-peak, odd-Z, and s-process elements, and we found that the evolution of P in the disk most strongly resembles that of the α-elements. We also find that molar P/C and N/C ratios for our sample match the scatter seen from other abundance studies. Finally, we measure a $[\mathrm{P/Fe}] = 0.09 \pm 0.1$ ratio in one low-α halo star and probable Gaia–Sausage–Enceladus member, an abundance ratio ∼0.3–0.5 dex lower than the other Milky Way disk and halo stars at similar metallicities. Overall, we find that P is likely most significantly produced by massive stars in core-collapse supernovae, based on the largest P abundance survey to date.

Unified Astronomy Thesaurus concepts: Stellar abundances (1577); Galaxy chemical evolution (580)

Supporting material: machine-readable tables

1. Introduction

The only stable isotope of P (^{31}P) is thought to be created in multiple different nucleosynthesis channels. Empirical tests of these different production processes are limited by the few known stellar P abundances. A low galactic abundance of P (relative to the even-Z α-elements) and the lack of any detectable optical transitions in FGK-type stars have made large-scale abundance studies challenging. The first P chemical evolution study, totaling 20 stars, used P I lines spanning 10500–10600 Å in the infrared (IR) *Y* band (Caffau et al. 2011). Recently, additional studies have used the IR *Y*-band lines (Caffau et al. 2016; Maas et al. 2017; Caffau et al. 2019; Maas et al. 2019; Sneden et al. 2021; Sadakane & Nishimura 2022), UV P I lines at ∼2134 Å (Jacobson et al. 2014; Roederer et al. 2014, 2016; Spite et al. 2017), and lines in the IR *H* band from ∼15700–16500 Å (Hawkins et al. 2015; Afşar et al. 2018; Jönsson et al. 2018; Böcek Topcu et al. 2019; Masseron et al. 2020a; Jönsson et al. 2020).

These surveys combine for a total ∼190 P abundances, with an average of 21 stars per study. One notable exception is the APOGEE survey, which reports P abundances for tens of thousands of stars. However, the IR *H*-band lines are blended with other molecular features and impacted by telluric contamination, making P the most uncertain element with reported abundances in the APOGEE catalog, and therefore it should be used with caution (Hawkins et al. 2016; Jönsson et al. 2020). Nonetheless, the APOGEE survey has led to the discovery of P-rich stars (Masseron et al. 2020a). At higher resolutions, the IR *H*-band lines may be used for more precise P abundance measurements (e.g., with the IGRINS instrument; see Afşar et al. 2018; Böcek Topcu et al. 2019).

The initial ∼190 stellar P abundances have placed some constraints on galactic chemical evolution models. The *Y*-band lines can be used to study stars with $[\mathrm{Fe/H}] \gtrsim -1.3$, and the UV lines are best detected in metal-poor stars. The combination of these studies has demonstrated that hypernovae best describe the evolution of P at early epochs (Jacobson et al. 2014) and phosphorus abundances for stars spanning $-1 < [\mathrm{Fe/H}] < 0.5$ do not match chemical evolution models tuned for the solar neighborhood that include yields from CCSN, Type Ia SN, and asymptotic giant branch (AGB) stars (e.g., Cescutti et al. 2012; Maas et al. 2019). The current best-fitting model uses arbitrarily enhanced massive star yields from Kobayashi et al. (2006) to match existing measurements (model 8 in Cescutti et al. 2012). The limited number of P abundances has demonstrated that theoretical models are either missing additional P-production process, P yields must be increased, or possibly both.

While P is thought to be primarily created by neutron capture on Si during hydrostatic burning and released in core-collapse supernovae (CCSNe; Woosley & Weaver 1995), and an enhanced P abundance as been observed in the supernova remnant Cas A (Koo et al. 2013), other processes such as massive rotating stars (Prantzos et al. 2018) and C-O shell mergers within stars (Ritter et al. 2018) are promising methods

---

[*] Based on observations obtained with the Hobby–Eberly Telescope, which is a joint project of the University of Texas at Austin, the Pennsylvania State University, Ludwig-Maximilians-Universität München, and Georg-August-Universität Göttingen.

to enhance P yields. However, when these processes are utilized in chemical evolution models, they do not yet match the P abundances observed in the galaxy. Analysis of APOGEE abundances has suggested P may be made in Type Ia SN (Weinberg et al. 2019) or P may be made via proton capture in massive stars (Caffau et al. 2011). Additionally, P-rich stars have also challenged theoretical models; abundance patterns of these stars include enhanced Mg, Si, Al, and s-process elements but are not consistent with other chemically peculiar stars (e.g., CH stars; see Masseron et al. 2020a, 2020b). The unusual abundances suggest P-enriched stars may be from a new site of the s-process (Masseron et al. 2020b).

Beyond chemical evolution, P is an important element for life: phosphorus-bearing molecules make up the backbone of DNA/RNA (Schlesinger & Bernhardt 2013) and are key in energy transport between cells (Nelson & Cox 2017). However, of the key elements for life (the CHNOPS elements), phosphorus is the most poorly studied in stars (Jacobson et al. 2014; Hinkel et al. 2020). P is especially important because this element may be strongly partitioned in the cores of planets (Stewart & Schmidt 2007), so an underabundance of P relative to the solar value may impact the available surface P on exoplanets (Hinkel et al. 2020). While the chemical composition of exoplanet surfaces cannot be directly measured, in certain cases host star abundances can be used as a proxy (Thiabaud et al. 2015) and the first step to understanding the availability of P on other planets is to measure P in stars (Hinkel et al. 2020).

Understanding the chemical evolution of P in the galaxy, the nucleosynthesis sites of P, and the connection between P in stars and planets relies on stellar abundance measurements. To this end, we have measured stellar abundances in 163 stars using the HPF instrument on the Hobby–Eberly Telescope (HET), creating the largest survey of precise P abundances to date. Our observation sample selection is described in Section 2. Atmospheric parameter and abundance derivation methodologies are discussed in Section 3. Our key results, which include the galactic chemical evolution of P, likely important P nucleosynthesis processes, [P/Fe] comparisons between thin and thick disk stellar populations, and P abundances translated to molar fractions, are discussed in Section 4. Our primary conclusions are listed in Section 5.

2. Sample Selection and Observations

IR P I features have weak line strengths relative to other absorption lines (as shown by three representative HPF spectra in Figure 1) and are difficult to detect for stars with $-1.3 \lesssim$ [Fe/H] (Maas et al. 2019). The stellar sample was thus chosen to ensure the Y-band P I features were observable. Our target stars were selected from Bensby et al. (2014) and APOGEE DR16 (Jönsson et al. 2020). Stars with $J \lesssim 8$ mag were chosen from both surveys in order to minimize the exposure times necessary to achieve signal-to-noise ratios (S/Ns) over 100, which are required to detect the P I feature (e.g., Maas et al. 2019). The P I features in the Y band have high excitation potentials of ∼7 eV, and become difficult to detect in cool stars (e.g., Arcturus, Maas et al. 2017). We only selected stars with $T_{\rm eff} > 4500$ K, to ensure the P I feature was detectable and consistent with the $T_{\rm eff}$ range used in previous studies (Maas et al. 2017, 2019).

Observations were performed using the HPF spectograph (Mahadevan et al. 2012, 2014) on the HET. HPF is fiber-fed and observes an approximate wavelength range of 8000–13000 Å with a resolution (R) ∼50,000. Target stars were observed between 2020 August and 2020 December with metal-poor and/or thick disk targets, identified with [Fe/H] from Bensby et al. (2014) and Jönsson et al. (2020) as well as initial population memberships from Bensby et al. (2014), prioritized for observation. A total of 163 stars were observed with the HPF, with photometry, observation dates, S/Ns, and parallaxes given for each star in Table 1.

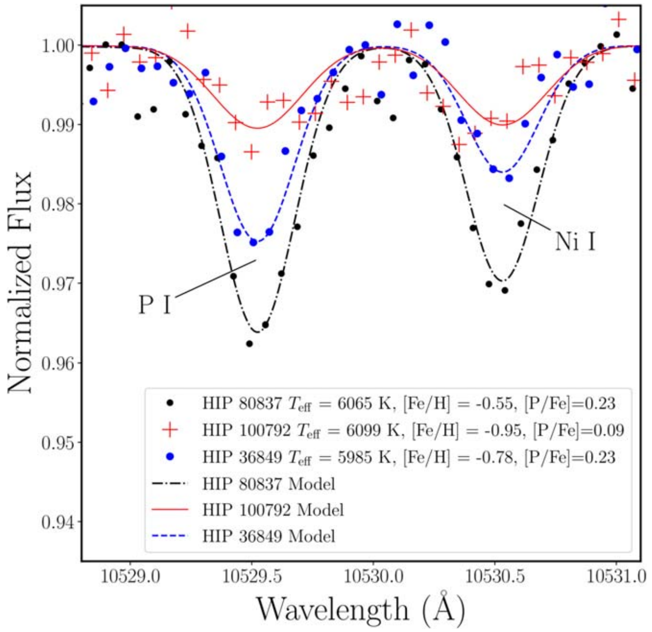

Figure 1. Three observations of relatively metal-poor stars with similar $T_{\rm eff}$ and log(g) from HPF on the HET are plotted with three synthetic spectra. The observed spectrum of HIP 80837 is represented as black circles, that of HIP 100792 is shown as red crosses, and that of HIP 36849 is shown as blue circles. Model spectra for these stars are displayed as a black dotted–dashed line, a red solid line, and a blue dashed line, respectively.

Data reduction was performed using the `Goldilocks` automatic pipeline.[6] The pipeline reduction steps follow Ninan et al. (2018) and can be summarized in the following steps: first, the bias level was subtracted using reference pixels on the edges of the detector. Next, nonlinearity corrections, a scattered light subtraction, and a flat-field correction were performed. Science and calibration images were extracted using a master trace image. The final data product included a sky fiber spectrum, target spectrum, errors, and wavelength solution for each star. We do not perform a telluric correction to maximize the final S/N. Previous analysis has shown spectra from the `Goldilocks` pipeline lead to accurate and precise stellar abundances (e.g., Sneden et al. 2021).

The strongest P I feature with no telluric contamination in the HPF spectrum is at 10529.52 Å and is the primary P I line used for abundance measurements in this study. Other lines are not available, due to gaps in the wavelength coverage or blends with telluric lines. Additionally, there are two sky emission lines relatively close to the P I features. Each object spectrum was visually inspected and the sky emission was corrected using a sky fiber spectrum when the lines were nearly blended with the 10529.52 Å P I feature. Only ∼10 stars required sky subtraction to remove contamination from or near the P I

---

[6] hydra.as.utexas.edu/?a=help&h=121

Table 1

Sample Parallaxes and Observation Summary

Name	Date Obs. (UT Date)	RA. deg.	DEC. (deg.)	Obs (S/N)	G (mag)	σG (mag)	BP (mag)	σBP (mag)	RP (mag)	σRP (mag)	VT (mag)	σVT (mag)	BT (mag)	σBT (mag)	J	σJ (mag)	H (mag)	σH (mag)	K$_s$ (mag)	σK$_s$ (mag)	W1 (mag)	σW (mag)	W2 (mag)	σW2 (mag)	π (mas)	σ π (mas)
HIP101346	2020-08-07	308.09979	6.51752	283.0	8.401	0.003	8.675	0.003	7.950	0.004	8.56	0.01	9.15	0.01	7.44	0.02	7.17	0.02	7.10	0.02	7.08	0.03	7.11	0.02	10.04	0.022
HIP102610	2020-08-21	311.90774	12.98616	209.0	7.296	0.003	7.590	0.003	6.825	0.004	7.50	0.01	8.13	0.01	6.28	0.02	5.97	0.02	5.91	0.02	5.87	0.05	5.82	0.03	24.94	0.018
HIP102838	2020-08-07	312.51246	7.85000	192.0	8.393	0.003	8.713	0.003	7.898	0.004	8.61	0.01	9.36	0.01	7.35	0.02	7.04	0.05	6.95	0.03	6.90	0.03	6.96	0.02	16.74	0.020
HIP103682	2020-08-27	315.14089	−4.72995	158.0	6.064	0.003	6.369	0.003	5.590	0.004	6.26	0.01	6.96	0.01	5.15	0.03	4.86	0.02	4.77	0.02	4.72	0.08	4.46	0.04	37.00	0.029
HIP103692	2020-08-02	315.18085	17.44797	116.0	7.895	0.003	8.230	0.003	7.388	0.004	8.13	0.01	8.91	0.01	6.82	0.03	6.53	0.05	6.48	0.02	6.44	0.04	6.46	0.02	17.55	0.021
HIP104659	2020-08-10	317.99626	17.72986	233.0	7.231	0.003	7.501	0.003	6.781	0.004	7.43	0.01	7.95	0.01	6.25	0.02	5.99	0.03	5.94	0.02	5.91	0.05	5.84	0.02	29.88	0.020
HIP104672	2020-08-22	318.03117	10.63799	129.0	7.948	0.003	8.222	0.003	7.502	0.004	8.13	0.01	8.74	0.01	7.03	0.02	6.78	0.03	6.69	0.02	6.68	0.04	6.70	0.02	12.74	0.023

Note. Sources of photometry and parallax: J, H, and K$_s$ from 2MASS (Skrutskie et al. 2003, 2006); VT and BT from ESA (1997) and Høg et al. (2000); W1 and W2 photometry from WISE (Wright et al. 2010, 2011); and G, BP, RP, parallax (π), and parallax uncertainty from Gaia eDR3 (Gaia Collaboration et al. 2016, 2021).

(This table is available in its entirety in machine-readable form.)

feature line profile. The spectra were normalized using a spline function with a sigma-clipping algorithm. The S/N of each spectrum was found by estimating the variance from featureless regions of the continuum near the P I feature.

3. Atmospheric Parameters

3.1. Methodology Overview

We required an atmospheric parameter derivation methodology that was applicable to both cool K giants and F dwarfs. Typical iron line excitation analysis (e.g., Fe I versus Fe II) to derive $T_{\rm eff}$ and log(g) were difficult to adapt for the Y-band spectra, as there are few detectable Fe II lines, especially for the cool K giants, within the observed spectral range 8000–13000 Å (Kondo et al. 2019; Sneden et al. 2021). Additionally, while there has been significant progress in Y-band abundance methodologies (e.g., Caffau et al. 2019; Kondo et al. 2019; Matsunaga et al. 2020; Fukue et al. 2021; Sneden et al. 2021), atomic line data have not been experimentally validated at the same level as for optical wavelengths. We therefore combine information from multiple surveys to determine the atmospheric parameters using photometry, parallaxes, and finally equivalent width measurements of Fe I lines in our spectral range.

The effective temperature, surface gravity, and their uncertainties were calculated using the MINESweeper spectrophotometric modeling tool[7] (Cargile et al. 2020). The software is capable of simultaneously fitting an observed stellar spectrum and isochrones to predict various stellar atmospheric parameters using a dynamic nested sampler (Speagle 2020). `MINESweeper` has been validated using multiple star clusters (Cargile et al. 2020) and has been used to determine parameters for the H3 survey (Conroy et al. 2019). We only utilized the photometric fitting capabilities, due to the added uncertainties found when deriving atmospheric parameters broadly from Y-band absorption features. MINESweeper makes use of MESA Isochrones and Stellar Tracks (MIST; Choi et al. 2016), which were created using the Modules for Stellar Astrophysics (MESA) software suite (Paxton et al. 2011). MINESweeper also utilizes `ThePayne` (Ting et al. 2019) to interpolate between different stellar models. Finally, MINESweeper uses ATLAS model atmospheres (Kurucz 1979, 2013), which are consistent with MARCS models for the metal-rich FGK stars considered in this study (Gustafsson et al. 2008).

3.2. Input Data and Parameters For MINESweeper

We use sets of photometric data spanning from the optical to the infrared to derive the stellar atmospheric parameters. Optical photometry from Gaia eDR3: G, BP, and RP, (Gaia Collaboration et al. 2016, 2021), the Tycho survey: VT and BP (ESA 1997; Høg et al. 2000), 2MASS: J, H, K_s (Skrutskie et al. 2003, 2006), and WISE: W1 and W2 (Wright et al. 2010, 2011) were used with MINESweeper. Following Cargile et al. (2020), an error floor of 0.01 mag was applied to photometric measurements to ensure the uncertainties were not underestimated. A Gaussian prior was set with the mean and standard deviation equal to the Gaia eDR3 parallaxes and uncertainties, respectively (Gaia Collaboration et al. 2021), for our sample stars.

Table 2
Line List

Wavelength (Å)	Line ID	χ (eV)	Log(gf)	Source
8207.742	Fe I	4.446	–0.960	(1)
8339.402	Fe I	4.473	–1.100	(1)
8360.794	Fe I	4.473	–1.100	(1)
8471.743	Fe I	4.956	–0.910	(1)
8514.072	Fe I	2.198	–2.227	(1)
8571.804	Fe I	5.010	–1.110	(1)
8582.257	Fe I	2.990	–2.133	(1)
8598.829	Fe I	4.387	–1.182	(1)
8610.610	Fe I	4.435	–1.690	(1)
8674.746	Fe I	2.832	–1.783	(1)
8699.454	Fe I	4.956	–0.370	(1)
8824.220	Fe I	2.198	–1.540	(1)
8876.024	Fe I	5.0200	–1.100	(1)
10216.313	Fe I	4.7330	–0.062	(2)
10395.796	Fe I	2.1760	–3.390	(2)
10529.524	P I	6.949	0.24	(3)

References. (1) Heiter et al. 2021; (2) Placco et al. 2021; (3) Berzinsh et al. 1997.

The photometric data and parallaxes are given in Table 1. We performed an initial MINESweeper run with the input parameters and an [Fe/H] prior set from $-1 < [{\rm Fe/H}] < 0.2$. A flat prior on dust extinction was also set at $0 < A_v < 0.2$ mag for all but one star, HD 25532, which the Python package `dustmaps` (Green et al. 2019) predicts to have a high extinction of $A_v \sim$0.35 mag. Increasing the flat prior boundary to 0.5 mag brought atmospheric parameters for that one star in agreement with literature measurements. We also corrected the Gaia eDR3 parallax zero points using the prescription from Lindegren et al. (2021). The average offset and standard deviation was $--0.033 \pm 0.003$ mas. We applied the average offset for stars that had two-point astrometric solutions, and we found the parallax offset was not a significant source of uncertainty for our sample of stars.

Next, we measured [Fe/H] ratios using Fe I lines equivalent widths from lines successfully used in Sneden et al. (2021). Equivalent widths were measured by fitting Gaussian profiles to absorption features with the spectrum analysis code `iSpec` (Blanco-Cuaresma et al. 2014; Blanco-Cuaresma 2019). All lines were crossmatched with a telluric catalog within `iSpec`, and features with significantly blended with telluric lines were removed. The equivalent width measurements were tested using Fe I lines from a twilight spectrum with an S/N of ∼300. We measured an $A({\rm Fe\ I})_\odot = 7.46 \pm 0.05$ with a microturbulence (ξ) of 0.67 km s^{-1} using a MARCS model atmosphere built to match the Sun ($T_{\rm eff}$ 5777 K and log(g) = 4.44 dex). The Fe I abundance is consistent with previous solar Fe abundance measurements (Asplund et al. 2009), and our Fe I line list is given in Table 2.

The Fe I abundance for each star was calculated using the local thermodynamic equilibrium (LTE) radiative transfer code MOOG (Sneden 1973) with 1D MARCS atmospheric models (Gustafsson et al. 2008). We used plane-parallel model atmospheres for stars with $\log(g) > 3.5$ dex and spherical models for stars with $\log(g) < 3.5$ dex. The initial MARCS model atmospheric parameters were set to the MINESweeper output $T_{\rm eff}$, log(g), [Fe/H], and an assumed microturbulence of 1.0 km s^{-1}. We then calculated the Fe I abundances with MOOG and proceeded to perform a grid search over potential microturbulence values to find which best

---

[7] github.com/pacargile/MINESweeper

Table 3
Atmospheric Parameter and Abundances

Name	$T_{\rm eff}$ (K)	$\sigma T_{\rm eff}$ High (K)	$\sigma T_{\rm eff}$ Low (K)	log(g) (dex)	σ log(g) (dex)	[Fe/H] (dex)	σ [Fe/H] (dex)	ξ (km s^{-1})	[P/Fe] (dex)	σ [P/Fe] (dex)
HIP101346	6012	94	76	3.99	0.02	–0.45	0.08	1.09	0.09	0.05
HIP102610	5902	60	89	4.27	0.02	–0.11	0.08	0.89	–0.01	0.05
HIP102838	5611	71	34	4.27	0.02	–0.29	0.06	0.82	0.42	0.06
HIP10306	6409	92	99	3.89	0.02	–0.34	0.06	1.85	0.09	0.03
HIP103682	5973	39	56	4.27	0.01	0.47	0.06	0.61	–0.12	0.05
HIP103692	5708	77	77	4.21	0.02	0.29	0.09	1.26	0.04	0.08
HIP104672	6114	37	62	4.11	0.02	–0.07	0.10	1.62	0.06	0.05

Note. A solar Fe abundance of $A(\mathrm{Fe})_\odot = 7.5$ was adopted from Asplund et al. (2009), and the value of $A(\mathrm{P})_\odot = 5.43$ is from this work (see Section 3.4). The microturbulence (ξ) uncertainties are discussed in 3.2.

(This table is available in its entirety in machine-readable form.)

removes any differences in Fe I abundance for both strong and weak lines. However, for giant stars, additional lines with lower excitation energies became saturated at lower effective temperatures, ergo they were not used in calculating the final [Fe/H] abundance. We therefore did not calculate the microturbulence using Fe I line equivalent widths for giant stars, because the number of stronger Fe I lines was limited. We instead adopted the methodology of APOGEE DR13 (Holtzman et al. 2018) and used an empirical relationship between the microturbulence and log(g), given in Equation (1), for stars with $\log(g) < 3.5$ dex:

$$\log(\xi) = 0.225 - 0.0228(\log(g)) + 0.0297(\log(g))^2 - 0.0113(\log(g))^3 . \quad (1)$$

We then reran MINESweeper with the new Fe I abundance, and an Fe I prior equal to the [Fe/H] uncertainty. After the second iteration, we removed any lines that gave an $A(\mathrm{Fe}) > 0.2$ dex from the average values, to remove outliers that may have been impacted by unflagged telluric lines or were saturated. We iterated this process multiple times until the parameters no longer changed with each iteration. Often, the parameters did not significantly change after two iterations. The final atmospheric parameters and uncertainties are given in Table 3.

The uncertainties on $T_{\rm eff}$ and log(g) are derived from the output posterior distributions from MINESweeper. The mean A(Fe I) abundance from the lines used in Table 2 is taken to be the final iron abundance. The uncertainty on the [Fe/H] ratio is the standard deviation from the set of line equivalent width measurements for star in our sample. We estimated the uncertainty on the microturbulence for stars with $\log(g) > 3.5$ dex by finding which microturbulence value corresponds to the 1σ uncertainty on the slope of the fit to the logarithm of the line strength and Fe I line abundance. The average uncertainty is 0.25 ± 0.1 km s^{-1} from this methodology. We also propagated the errors in Equation (1) for a $\log(g) = 3 \pm 0.1$ dex. We find an uncertainty of 0.14 km s^{-1}, although this error propagation does not include uncertainty on the polynomial fit coefficients. We therefore adopt an error of 0.25 km s^{-1} for all stars in our sample. The iron abundance for each star was then normalized with solar abundances from Asplund et al. (2009), $A(\mathrm{Fe})_\odot = 7.5$. The default solar abundances used for MOOG v. 2019 are Asplund et al. (2009) abundances, and therefore we normalized our Fe abundances with this scale. The final atmospheric parameters are listed in Table 3.

3.3. Atmospheric Parameter Comparisons

We tested the accuracy and precision of our atmospheric parameter methodology by comparing our results to previous literature studies, namely Bensby et al. (2014) and APOGEE DR16 (Jönsson et al. 2020), the primary sources for our sample selection. Additionally, a significant fraction of our stars have been analyzed in other literature studies, and so we also make comparisons to the PASTEL catalog (Soubiran et al. 2016) and a reanalysis of Geneva–Copenhagen targets (Casagrande et al. 2011). For the PASTEL catalog, the effective temperatures and log(g) values used for comparison were the averages for all the entries from different literature sources for each star. The comparison of the atmospheric parameters is shown in Figure 2.

We found our calculated atmospheric parameters to be consistent with literature samples for the FGK sample from Bensby et al. (2014), as quantified in Table 4. The $T_{\rm eff}$ systematic differences are $\lesssim$–30 K or less, and with standard deviations that are similar to the measurement uncertainties for each study. For example, stars from this work had an average $\sigma\, T_{\rm eff} = 62$ K and the average $\sigma\, T_{\rm eff} = 72$ K from Bensby et al. (2014) for stars in common. These $T_{\rm eff}$ uncertainties added in quadrature yield a value of 95 K, which is similar to the differences seen between both studies in Table 4. Some stars in our sample saturate in one or more of the 2MASS filters, which may be the cause of some of the systematic differences observed. We compare stars with only stars with all "AAA" 2MASS quality flags, indicating that J, H, and K$_s$ were all reliable measurements and not saturated on the detector. The stars with poor photometry are highlighted in Figure 2, and removal of these stars only slightly improves the differences between the different sets of parameters found in the literature. For example, the $\langle T_{\rm eff} \rangle$ offset improves by 10 K for the stars in common with Bensby et al. (2014; shown in Table 4). We do find log(g) differences much larger than our reported error, and assume a conservative $\sigma\log(g) = 0.1$ dex when determining the errors of our [P/Fe] ratios from the uncertainty of the atmospheric parameters (in Section 3.5).

The stars selected from APOGEE DR16 have greater differences between our results and the parameters from Jönsson et al. (2020). However, these systematic differences are similar in size when APOGEE results are compared to other abundance surveys (Jönsson et al. 2018). The largest difference is in surface gravity; however, the P I lines are relatively unaffected by changes in log(g) compared to changes in $T_{\rm eff}$

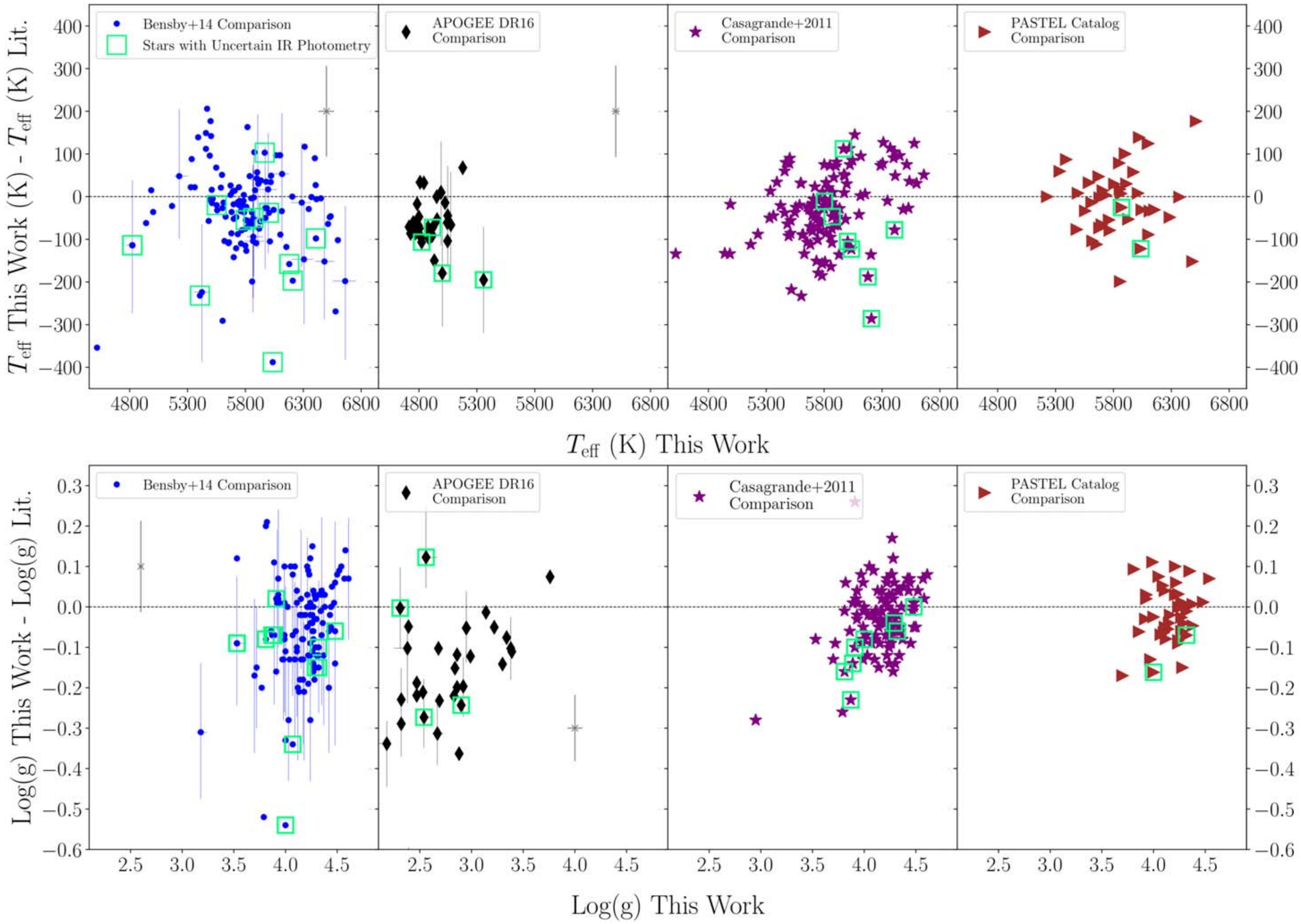

Figure 2. From left to right, panels show a comparison of this work to that of Bensby et al. (2014) as blue circles, to APOGEE DR16 (Jönsson et al. 2020) as black diamonds, to Casagrande et al. (2011) as magenta stars, and to the PASTEL catalog as brown triangles (Soubiran et al. 2016). The top panels show the differences in derived effective temperature, and the bottom panels show differences in log(g). Error bars are only shown for stars with errors above 1σ from the average uncertainty on the parameter difference for the Bensby et al. (2014) and APOGEE DR16 comparisons. We also include representative error bars as gray "x" symbols in the APOGEE DR16 and Bensby et al. (2014). Light green boxes highlight stars with highly uncertain (>0.2 mag) 2MASS photometry for two or more filters.

and the uncertainty on the synthetic spectrum fits (e.g., uncertainties in Maas et al. 2019 and values listed in Table 5).

We also compare our derived [Fe/H] ratios to previous studies in Figure 3 and statistics in Table 4. We do not test our [Fe/H] ratios with the PASTEL catalog, to avoid averaging [Fe/H] abundance measurements from different methodologies and complicating interpretations of potential systematic uncertainties with our method. We use Fe I abundances from Bensby et al. (2014) to match our methodology, and renormalize all literature results to the Asplund et al. (2009) solar scale. We find no significant systematic offsets, and the uncertainties are similar to our quoted measurement uncertainties. Since we specifically compare other Bensby et al. (2014) abundances to P in Section 4.3, we perform a linear regression on the [Fe/H] differences versus [Fe/H] from this work (left panel of Figure 3) to look for systematic uncertainties between methodologies. We find a slope of 0.00 ± 0.02, with a p-value $= 0.89$, indicating there is no statistically significant slope when comparing the [Fe/H] difference versus [Fe/H]. This suggests our [Fe/H] derivation methodology is consistent with Bensby et al. (2014) for both the metal-rich and metal-poor stars in our sample.

3.4. Solar P Abundance

We obtained a twilight spectrum from the HPF on the HET, to compare our Fe (discussed in Section 3.2) and P derivation methodology to the solar values. While the telluric lines are strengthened in the twilight spectrum, the P I line profile was not contaminated and the line profile was symmetric. We measured the solar phosphorus abundances using the P I line and calculated the uncertainty on the synthetic spectrum fit. We found an $A(P)_\odot = 5.43 \pm 0.02$, which is slightly less than the value of 5.46 from Caffau et al. (2007), greater than the measurement of 5.41 from Asplund et al. (2009), and matches the solar system values of $A(P) = 5.43$ dex (Lodders 2021). We therefore adopt a solar phosphorus abundance of $A(P)_\odot = 5.43$ dex.

Previous studies have found systematic differences between twilight solar spectra and reflected light spectra, specifically a 0%–4% decrease in line depth depending on the angular distance from the Sun (Gray et al. 2000), and a 1%–2% decrease with UVES data (Molaro et al. 2008). The equivalent widths for affected lines are also thought to decrease by similar percentages (Gray et al. 2000). A 1% or 4% increase in line strength would lead to an abundance change of 0.004 dex or 0.02 dex, respectively. The effects on the solar abundance from

Table 4
Atmospheric Parameter Comparisons

Lit. Source	Mean Δ $T_{\rm eff}$ (K)	σ Δ $T_{\rm eff}$ (K)	Mean Δlog(g) (dex)	σ Δ log(g) (dex)	Mean Δ [Fe/H] (dex)	σ Δ[Fe/H] (dex)	Ref.
Bensby+14	–31	99	−0.06	0.12	–0.03	0.10	(1)
Casagrande+11	–28	84	−0.04	0.11	0.02	0.11	(2)
PASTEL Catalog	–1	84	–0.01	0.07	⋯	⋯	(3)
APOGEE DR16	–58	58	–0.16	0.14	0.05	0.08	(4)
Stars with Precise 2MASS Photometry							
Bensby+14	–21	92	–0.04	0.10	–0.02	0.09	(1)
Casagrande+11	–27	78	−0.03	0.11	0.02	0.10	(2)
PASTEL Catalog	2	76	0	0.07	⋯	⋯	(3)
APOGEE DR16	–30	42	–0.16	0.17	0.06	0.08	(4)

Notes. The stars with precise IR photometry only include stars with two or more good JHK photometries (errors < 0.2 mag). The listed differences are literature values subtracted from this work (e.g., $[{\rm Fe/H}]_{\rm This\ Work}$ - $[{\rm Fe/H}]_{\rm Literature}$)

References. (1) Bensby et al. (2014); (2) Casagrande et al. (2011); (3) Soubiran et al. (2016); (4) Jönsson et al. (2020).

Table 5
Average Phosphorus Abundance Uncertainties

	⟨δ[P/Fe]⟩ (dex)	σ (δ[P/Fe]) (dex)
$T_{\rm eff}$ Upper	0.03	0.01
$T_{\rm eff}$ Lower	0.03	0.01
log(g)	0.03	0.01
[Fe/H]	0.01	0.01
ξ	0.01	0.03
Fit Upper	0.04	0.01
Fit Lower	0.04	0.01

Note. Average abundance uncertainties due to errors in various parameters were calculated independently and represented as ⟨δ[P/Fe]⟩.

use of a twilight spectrum are likely minimal in the specific case of the weak P I line compared to the uncertainty on the fit, but other solar abundances were not derived using the twilight spectrum.

3.5. Phosphorus Abundance Methodology

Phosphorus abundances were measured by fitting synthetic spectra to the 10529.52 Å feature. The wavelength, excitation potential (χ), and log(gf) values for the P I absorption line were adopted from Berzinsh et al. (1997) and are listed in Table 2. Synthetic spectra were generated using MOOG (Sneden 1973) and MARCS atmospheric models (Gustafsson et al. 2008). Each spectrum was shifted to the rest frame before abundance analysis using radial velocity and barycentric corrections derived from template matching within `iSpec` (Blanco-Cuaresma et al. 2014; Blanco-Cuaresma 2019). Some stars rotate rapidly enough that additional smoothing was required. We adopted projected rotation velocities from the Geneva–Copenhagen survey (Holmberg et al. 2007) for stars with v sin i $\geqslant 5\,{\rm km\,s}^{-1}$. Stars with smaller reported rotation speeds did not have their abundances change significantly when the v sin i was included in the fit. A grid of synthetic spectra of the P I line were created in steps of 0.01 dex, over a range of $-1 <$ [P/Fe] (dex) < 1.5. The best-fitting model was chosen using χ^2 minimization, and examples of model spectra are shown for three stars in Figure 1. The final, best-fitting phosphorus abundances for each star are listed in Table 3.

The uncertainty on the model fit is estimated with a Monte Carlo method; the observed fluxes are varied using Gaussian random numbers with standard deviations equal to the S/N of the spectrum at 10600 Å, following the methodology of Maas et al. (2019). The model then is refit, the process is repeated for 10,000 iterations, and the abundances at the 16% and 84% percentiles of the distribution are taken as the 1σ uncertainties.

We also estimated the impact from the uncertainties on the atmospheric parameters on the fitted abundance. We created separate models at the $\pm\,1\sigma$ level for each of the atmospheric parameters. For example, if a star had an $T_{\rm eff} = 6000{\rm K} \pm 100{\rm K}$, we would create models at 5900 and 6100K, determine the best-fitting synthetic spectrum in a newly created grid, then use the differences to the [P/Fe] ratio at 6000K to determine the uncertainties. We assume the uncertainties are independent of each parameter, and we add the final values in quadrature. The most dominant sources of uncertainty is from the model fit, as shown in Table 5.

We also examined how [P/Fe] ratios vary as a function of the stellar $T_{\rm eff}$. A relationship between $T_{\rm eff}$ and our abundance measurements can reveal unknown systematic effects from our abundance measurement methodology, such as deviations from LTE, or from difficulties with the line list (e.g., unidentified blends). We find no significant change in [P/Fe] ratios across our $T_{\rm eff}$ range, as shown in Figure 4. Other studies of similar P I features in the *Y* band have found little difference in [P/Fe] ratio for Hyades dwarfs and giants, consistent with our results (Maas et al. 2019). Additionally, consistent [P/Fe] ratios for stars spanning 4700–6700 K suggest no detectable, $T_{\rm eff}$-dependent, unidentified blend is likely affecting the 10529.52 Å line.

We compare our P abundances to measurements from the literature, including 12 stars with reported [P/Fe] ratios from APOGEE DR16 (Jönsson et al. 2020), and plot the differences in Figure 5. There are six stars in common with other *Y*-band P I studies: three from Caffau et al. (2011; HIP 10306, HIP 23941, and HIP 107975), two from Maas et al. (2019; HIP 174147 and HIP 38625), and one from Maas et al. (2017; HIP 174160). We compare our abundances from Table 3 with the values from those studies in Figure 5. We do not include a comparison with HIP 38625, since the [P/Fe] uncertainty from Maas et al. (2019) is 0.22 dex. We removed the solar normalization and ratio to [Fe/H], to ensure that only comparisons of the phosphorus abundances were examined between the various studies. In the

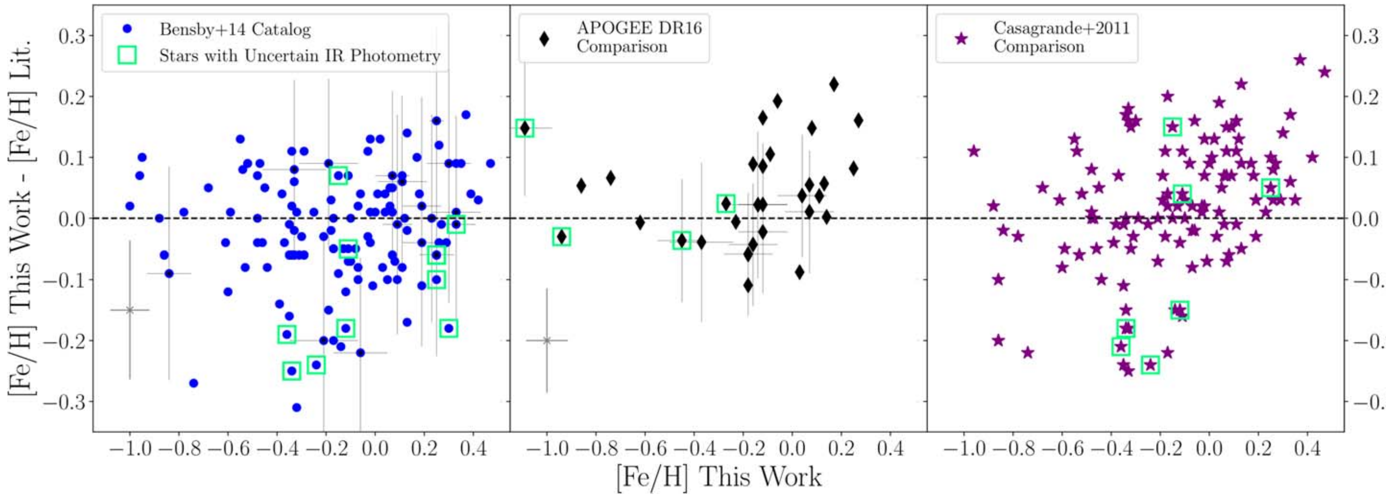

Figure 3. Comparison of literature [Fe/H] abundance measurements to results from this paper. The symbols here have the same meanings as those in Figure 2.

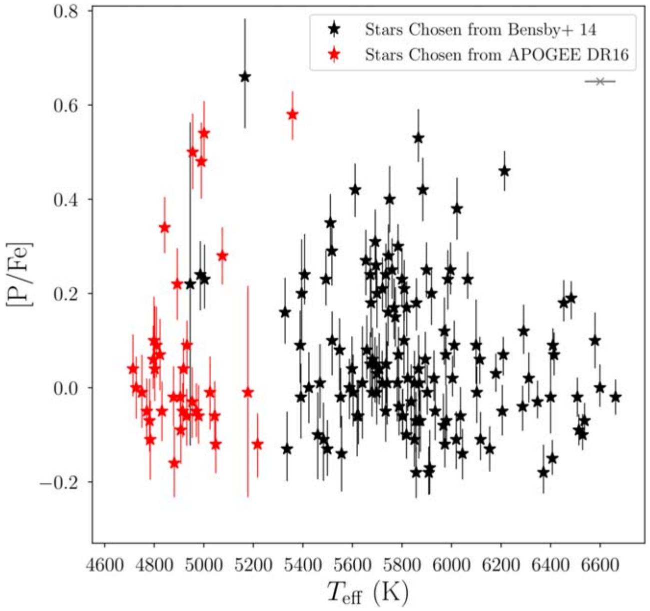

Figure 4. Comparison of [P/Fe] to $T_{\rm eff}$ from this work. Black stars are targets selected from Bensby et al. (2014), and red stars are those chosen from APOGEE DR16. The gray "x" in the upper right corner is a representative error bar for $T_{\rm eff}$.

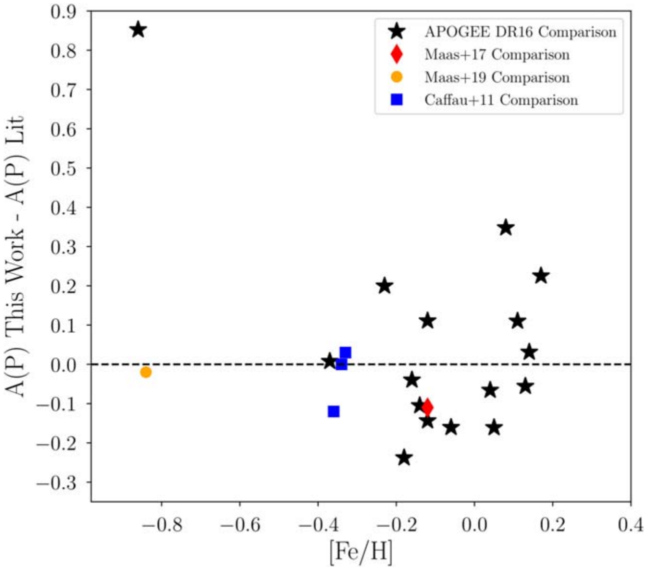

Figure 5. A(P) abundances from this study compared to those from APOGEE DR 16 (black stars), from Maas et al. (2017; red diamonds), from Maas et al. (2019; orange circle), and from Caffau et al. (2011; blue squares).

case of APOGEE DR16, we adopt an $\mathrm{A(P)}|_{\odot} = 5.36$ from Grevesse et al. (2007), then apply a correction of 0.183 dex from Table 4 of Jönsson et al. (2020) to match solar metallicity stars in the solar neighborhood. We find an average difference of -0.04 ± 0.06 dex for the five P I values, and for APOGEE we find a difference of 0.0 ± 0.17 dex, excluding the one outlier star, HD 81762. A larger sample is needed in order to conduct a more detailed comparison with APOGEE.

4. Discussion

4.1. Comparing Thin Disk to Thick Disk Stars

Abundances differences between the thin and thick disk stars exist for the α-elements, indicative of the different chemical histories of each population of stars in the Milky Way (e.g., Edvardsson et al. 1993; Bensby et al. 2014; Hayden et al. 2015). We examined whether phosphorus behaved similarly to the α-elements in the thin and thick disk for our stars, as suggested by Maas et al. (2019). To do this, we first derived U, V, and W velocities for each of our stars using Gaia eDR3 positions, parallaxes, proper motions, and radial velocities (Gaia Collaboration et al. 2021) with the `pyia` code (Price-Whelan 2018) in order to properly account for the correlated uncertainties on the final galactocentric velocity components.

We generated 1000 sample parameters for each star using the Gaia covariance matrices, computed the resulting positions and velocities in the galactocentric frame, and adopted the standard deviation and mean values as the best sets of velocities and associated uncertainties using `pyia` (Price-Whelan 2018). The coordinate transformation into the galactocentric frame was calculated using `astropy` Python package (Astropy Collaboration et al. 2013). Finally, the velocities were corrected to the local rest frame by removing a rotation velocity of 238 km s^{-1} (Marchetti et al. 2018).

The galactocentric velocities were then used to determine the likely stellar population assignment for each sample star using the methodology of Ramírez et al. (2013). The use of

Table 6
Stellar Kinematics and Galactic Population Membership Probabilities

Star Name	U (km s^{-1})	σ U (km s^{-1})	V (km s^{-1})	σ V (km s^{-1})	W (km s^{-1})	σ W (km s^{-1})	P(Thin Disk)	P(Thick Disk)	P(Halo)
HIP101346	–40.6	0.2	–14.6	0.2	–0.5	0.1	0.99	0.01	0.00
HIP102610	−10.3	0.1	−15.0	0.1	18.8	0.1	0.99	0.01	0.00
HIP102838	−96.2	0.1	−45.0	0.1	14.2	0.1	0.69	0.30	0.00
HIP103682	5.8	0.1	−16.8	0.1	4.6	0.1	0.99	0.01	0.00
HIP103692	5.8	0.1	−16.8	0.1	4.6	0.1	0.99	0.01	0.00
HIP104672	−61.3	0.1	−44.8	0.1	−10.9	0.1	0.88	0.12	0.00

Note. UVW values are galactocentric velocities corrected to the local standard of rest.

(This table is available in its entirety in machine-readable form.)

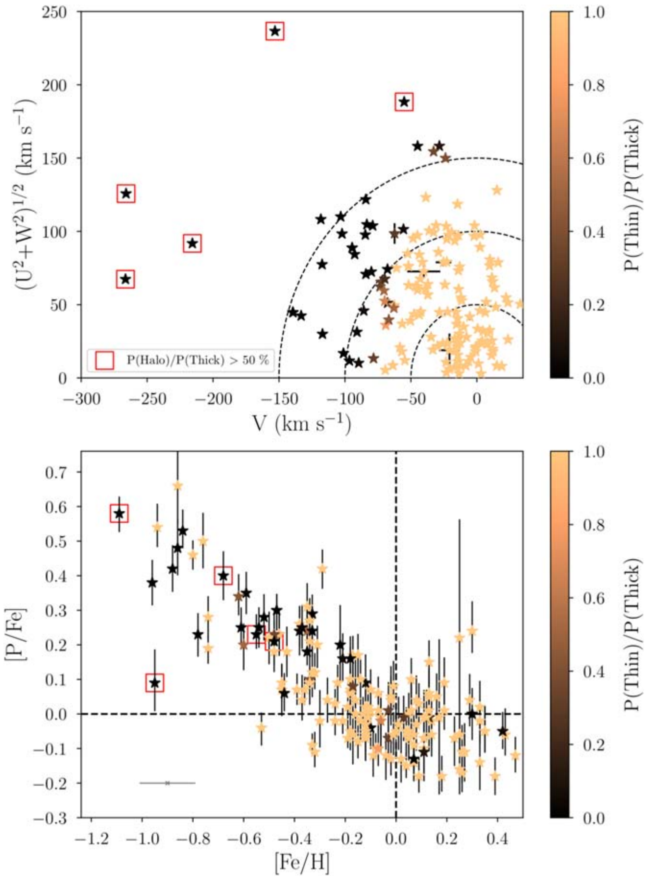

Figure 6. Top panel: the galactocentric velocity V and the sum of the squares of the U and W velocity components are plotted for the observed stars. Dashed lines represent radii at 50 km s^{-1}, 100 km s^{-1}, and 150 km s^{-1}. Bottom panel: [P/Fe] ratio compared to the [Fe/H] ratio. In both panels, the color bar represents the thin disk to thick disk probability ratio, with black stars being likely thick disk members and gold stars probable thin disk stars. The gray "x" in the bottom left corner is a representative [Fe/H] error bar. Stars in red boxes have halo-to-thick-disk probabilities above 50%.

galactocentric velocities to identify thin disk, thick disk, and halo stars is consistent with other methods in the literature (e.g., Bensby et al. 2014) and has given results similar to those of abundance studies that have derived population probabilities using orbital parameters (Franchini et al. 2020). The UVW velocities, thin disk, thick disk, and halo membership probabilities are listed in Table 6. A Toomre diagram and the [P/Fe] versus [Fe/H] relation with thin/thick disk color-coding are shown in Figure 6.

We made selection cuts to quantify any difference between the two stellar populations. Following Bensby et al. (2014), we selected stars with P(Thin)/P(Thick) > 10 for thin disk stars and P(Thin)/P(Thick) < 0.1 for thick disk stars, to ensure stars with inconclusive population probabilities did not affect the analysis. We examined the metallicity range between –0.9 < [Fe/H] < –0.1, where the [α/Fe] ratio begins to diverge between thin and thick disk stars but before [α/Fe] plateaus at low [Fe/H] ratios. We also recalculated UVW velocities given in Table 4 of Maas et al. (2019) with the methodology above, and added those stars to the sample in order to increase the number of stars used in the analysis. We made a final cut on [Fe/H] uncertainty and removed stars with high [Fe/H] uncertainties (σ[Fe/H] > 0.1 dex).

We show the resulting sample of stars in Figure 7. Initial inspection reveals a small difference between thin and thick disk stars, although there is scatter in the data. We fit a linear line to the thin and thick disk abundance ratios, to trace the evolution of phosphorus in each population. The best-fitting model was calculated using a Markov Chain Monte Carlo simulation performed using the `emcee` package (Foreman-Mackey et al. 2013).

We used 10,000 steps with 50 walkers, and the fits are shown as dashed lines in Figure 7. The resulting slope and intercept parameters for thin disk and thick disk stars are given in Table 7. The reported uncertainties are the 16% and 84% percentiles on the posterior distribution of each quantity. We recompute the linear fit using only the stars from this work, and find that the thin disk slope flattens and all quantities are more uncertain. However, a [P/Fe] difference between both stellar populations is still found.

We have also found that the [P/Fe] ratio decreases with increasing [Fe/H] at similar rates for both populations. We compute the 2σ confidence intervals (CIs) using the combined abundances from this work and from Maas et al. (2017, 2019). The CIs are plotted in Figure 7, and we find that that the difference between both fits exceeds the 2σ CIs between –0.57 < [Fe/H] < –0.13, although it is not significant at the 3σ level. Beyond this metallicity range, we lack enough measurements to confirm any offset from thin disk and thick disk stars. From our linear fitting parameters, we measure a [P/Fe] offset of 0.11 dex between both populations. The chemical evolution model of Kobayashi et al. (2011) predicts an offset between thin and thick disk stars of approximately 0.1 dex, similar to the observed value. The difference in [P/Fe] ratio between the thin and thick disk is similar to the behavior of other α-elements and suggest P is produced in CCSNe.

4.2. The Galactic Evolution of Phosphorus

Our phosphorus abundance ratio measurements are shown in Figure 8 and compared with chemical evolution models from

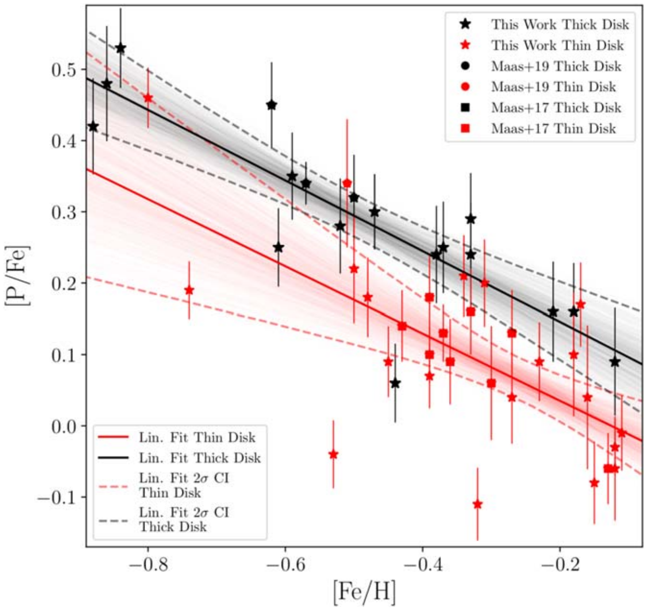

Figure 7. [P/Fe] vs. [Fe/H] from multiple studies. Stars that are highly likely thin disk members (red points) and thick disk members (black points) are plotted (as defined in Section 4.1). Red and black lines are linear fits (lin. fits) to the thin disk population and thick disk population, respectively, dashed lines represent the 2σ confidence intervals, and the fainter lines represent 1,000 samples from the MCMC fit. Data from this work are represented as stars, data from Maas et al. (2017) are squares, and data from Maas et al. (2019) are circles.

Cescutti et al. (2012), Prantzos et al. (2018), and Ritter et al. (2018) to further test if P behaves similarly to the α-elements. Each model has different assumptions on phosphorus yields and has been tuned to match stars in the solar neighborhood. The best-fitting model is from Cescutti et al. (2012), which includes massive star yields from Kobayashi et al. (2006), hypernovae, and a metallicity-independent P yield enhancement. However, additional abundance measurements in stars with metallicities between $-1.2 < [\mathrm{P/Fe}] < -0.5$ show the model underpredicts the [P/Fe] ratio at lower [Fe/H]. A solution more complicated than a metallicity-independent yield increase is therefore needed to explain the production of phosphorus in more metal-poor stars.

The Prantzos et al. (2018) model includes updated yields of massive rotating stars in addition to CCSN and Type Ia yields. While the addition of these yields has greatly improved models with other odd-Z elements (e.g., K), the Prantzos et al. (2018) model underproduces [P/Fe] and does not match the slope of the data. The C shell ingestion in convective O shells may also enhance the yields of the odd-Z elements in massive stars. Ritter et al. (2018) investigated how potential yield enhancements would affect chemical evolution models if 0%, 10%, 50%, and 100% of stars in the Galaxy had yields enhanced from the O-C shell interactions. Three of those models are plotted in Figure 8, and we find no model perfectly matches the slope of the [P/Fe] ratios as a function of metallicity (similar to Maas et al. (2019)). However, the 10% model approximately matches from $-0.6 < [\mathrm{Fe/H}] < -0.4$, and more enhanced yields are needed at lower metallicities.

In addition to chemical evolution models, we compare our abundances to different P abundance studies from multiple different surveys. We find our abundances are in general agreement with studies that used the IR *Y*-band and *H*-band P I features (Caffau et al. 2011; Maas et al. 2017, 2019; Sneden et al. 2021). The Caffau et al. (2019) abundances of stars near solar metallicity are, however, slightly offset from our abundance results. This survey uses *Y*-band IR features as well, and the discrepancy may be due to differences in atmospheric parameter choice or measurement methodology. Finally, we note that some high-[Fe/H] stars that utilize UV P I features are lower than our abundance ratios; however, the UV lines saturate and are highly uncertain near $[\mathrm{Fe/H}] \sim -0.2$ (Jacobson et al. 2014; Roederer et al. 2014).

4.3. The Evolution of Phosphorus Compared to Other Elements

We compared phosphorus abundances to α-elements, iron-peak elements, and s-process elements from Bensby et al. (2014) and Jönsson et al. (2020), to explore possible sites of P production. We chose to use abundances of other studies, due to the lack of O, Al, and s-process element lines in the *Y* band (e.g., Sneden et al. 2021). Different [P/X] ratio are plotted as a function of [Fe/H] in Figure 9.

α-Element Comparison: We compared phosphorus abundance measurements to O, Mg, Si, and Ca. We find that [P/O] increases with increasing metallicity, [P/Mg] is approximately constant from $-1.1 < [\mathrm{P/Mg}] < 0.5$, and [P/Si] (and [P/Ca] to an extent) are slightly decreasing with increasing [Fe/H]. Both Si and Ca are thought to be made in explosive burning in CCSN and have significant Type Ia contributions. The constancy with Mg and slight decreasing slope with Ca and Si suggests P is mostly made in CCSN, as expected from nucleosynthesis predictions.

Iron-peak Element Comparison: We compared phosphorus to Ni, Cr, and Zn (in addition to Fe in Figure 8). We find strongly decreasing [P/Cr] and [P/Ni], suggesting that P is made relatively quickly by massive stars and not in type Ia supernova, and it further resembles the evolution of the α-elements.

Odd-Z Element Comparison: We compared phosphorus to Na and Al, and found [P/Na] ratios increasing more significantly with [Fe/H] relative to [P/Al] ratios, where [P/Al] evolves more similarly to the α-elements. Na is thought to have strongly metallicity-dependent yields (Andrews et al. 2017) in massive stars, and phosphorus appears to have a different behavior over our [Fe/H] range.

S-Process Element Comparison: Finally, phosphorus abundance ratios with Y and Ba are explored. While there is significant scatter in the data, due to larger uncertainties on the s-process element abundances from Bensby et al. (2014), we still find [P/Y] and [P/Ba] ratios decrease with increasing metallicity. The [P/Y] and [P/Ba] ratios suggest that phosphorus does not correlate with disk star abundances of elements produced by the s-process in AGB stars.

We find that the evolution of P most closely resembles that of the α-elements, especially Mg, over our observed [Fe/H] range. The more significant the contributions of delayed processes, such as Type Ia SN and AGB stars production, the more strongly the [P/X] ratio decreases as [Fe/H] increases. Our abundance ratio comparisons are in agreement with our previous analysis that P is likely mostly produced in CCSNe.

4.4. Stars with Anomalous [P/Fe] Ratios

The [P/Fe] ratios for some of the stars in our sample are multiple standard deviations away from the average

Table 7
Thin Disk and Thick Disk Linear Fit Parameters

Sample	Slope	σ Slope High	σ Slope Low	Intercept (dex)	σ Intercept High (dex)	σ Intercept Low (dex)
Thin Disk: All Stars	–0.47	0.11	0.12	–0.06	0.03	0.03
Thick Disk: All Stars	–0.50	0.14	0.07	0.05	0.05	0.05
Thin Disk: This Work Only	–0.37	0.15	0.17	–0.05	0.03	0.04
Thick Disk: This Work Only	–0.46	0.24	0.08	0.03	0.05	0.05

Note. The designation "All Stars" includes those of Maas et al. (2017, 2019) that meet the criteria described in Section 4.1.

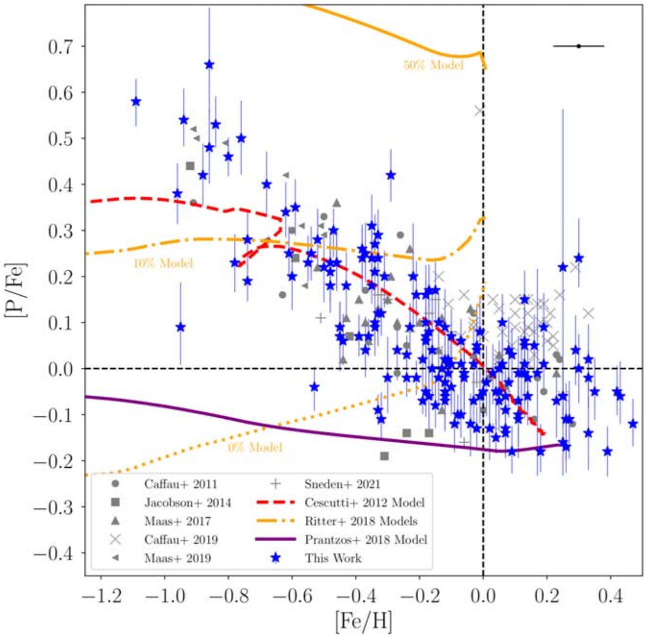

Figure 8. [P/Fe] vs. [Fe/H] ratios from this work (blue stars) as well as other studies (gray markers) are plotted. We include phosphorus abundance ratios from Caffau et al. (2011) as circles, from Jacobson et al. (2014) as squares, from Maas et al. (2017) as triangles, from Maas et al. (2019) as rotated triangles, from Caffau et al. (2019) as "x" symbols, and from Sneden et al. (2021) as "+" symbols. The solar abundance ratios are shown as black dashed lines, and the [Fe/H] representative error bar for this work is shown in the upper right of the plot. The chemical evolution model from Cescutti et al. (2012) is a red dashed line, and the model from Prantzos et al. (2018) is a purple solid line. Three Ritter et al. (2018) models with different numbers of stars undergoing C-O shell mergers are included as orange lines, with the 0% model as a dotted line, the 10% model as a dotted–dashed line, and the 50% model as a solid line.

phosphorus abundance for a given [Fe/H] ratio. We highlight three of these stars and discuss their possible origins.

4.4.1. HIP 100792

HIP 100792 star has been identified as a low-α member of the Galactic halo, suggesting the star is a member of an accreted system (Fuhrmann 1998; Nissen & Schuster 2010; Hawkins et al. 2015). Nissen & Schuster (2010, 2011) have also measured [Na/Fe] = –0.12 and an [Mn/Fe] = –0.25 for this star. These low Na and Mn abundances are characteristic of the accreted halo, especially for stars in the Gaia–Sausage–Enceladus (GSE) system (see Belokurov et al. 2018; Haywood et al. 2018; Helmi et al. 2018; Das et al. 2020). We also examine the kinematics of this star, specifically the vertical angular momentum component (L_z) and radial action (J_r), using the package `galpy` (Bovy 2015).

We found $L_z = –360.7$ kpc km s^{-1} and J_r=567.4 kpc km s^{-1} (or $\sqrt{J_r} = 23.8$ [kpc km s^{-1}]$^{\frac{1}{2}}$) using the potential `MWPotential2014` and the Staeckel approximation (described in Binney 2012). The kinematics agree with GSE kinematics from other studies (e.g., $J_r > 500$ kpc km s^{-1} and $L_z < 500$ kpc km s^{-1} from Yuan et al. 2020) and is nearly consistent with the selection criteria used in other GSE analyses, such as $30 \leqslant \sqrt{J_r} \leqslant 50$ (kpc km s^{-1})$^{\frac{1}{2}}$ and $–500 \leqslant L_z \leqslant 500$ kpc km s^{-1} (Feuillet et al. 2021; Buder et al. 2022). We note that the dynamical selection of GSE stars alone does not lead to a pure sample of GSE members, and can include up to ~20% non-accreted contaminants (Bonifacio et al. 2021). HIP 100792 therefore is chemically and dynamically similar to GSE stars, suggesting this star is likely a member of the same accreted population.

HIP 100792 has an [Fe/H] = –0.95 ± 0.09 with a [P/Fe] = 0.09 ± 0.1. This star is the only identified member of the low-α halo in our sample, and the [P/Fe] ratio is ~0.3–0.5 dex offset from similar thin and thick disk stars. The low P abundance for this one star is intriguing and motivates a larger P survey in accreted halo stars.

4.4.2. HIP 18833

HIP 18833 has an [Fe/H] = –0.53 ± 0.05 with a [P/Fe] = –0.04 ± 0.05. While the phosphorus abundance on the star is low, other chemical abundances do not suggested this is an accreted star. The [X/Fe] ratios for Mn, Al, and Na all appear characteristic of disk stars: [Mn/Fe] = –0.02 (Feltzing et al. 2007), [Na/Fe] = 0.07, and [Al/Fe] = 0.20 (Bensby et al. 2014), although [Al/Fe] has a large uncertainty of ± 0.18. The thin/thick disk probability ratio is also 63.6, indicating this star is very likely a thin disk member, based on kinematics. Finally, Bensby et al. (2014) find a [Mg/Fe] = 0.03 ± 0.11 for this star, similar to the [P/Fe] = –0.07 ± 0.05. The low abundance ratios suggests the low P abundance is likely related to the star's chemical history as opposed to an errant measurement.

4.4.3. HIP 95447

HIP 95447 has an [Fe/H] = 0.3 ± 0.07 with a [P/Fe] = 0.24 ± 0.08. The α-element abundance ratios for this star are not enhanced; for example, [Mg/Fe] = 0.02 ± 0.1 (Bensby et al. 2014). However, there is a large spread of $T_{\rm eff}$ for this star in the literature. The average $T_{\rm eff}$ in the PASTEL catalog is 5600 ± 147 K (Soubiran et al. 2016), and we found a $T_{\rm eff}$ of 5407^{+69}_{-34} K. HIP 95447 demonstrates some photometric and chromospheric variability as well (Lockwood et al. 2007). Broadband photometry may not reflect the star at its time of observation with HPF. A lower $T_{\rm eff}$ would require higher abundances to fit the P I line, potentially creating the offset. The most likely cause of an outlier [P/Fe] ratio for this star is an unknown systematic effect on the atmospheric parameters.

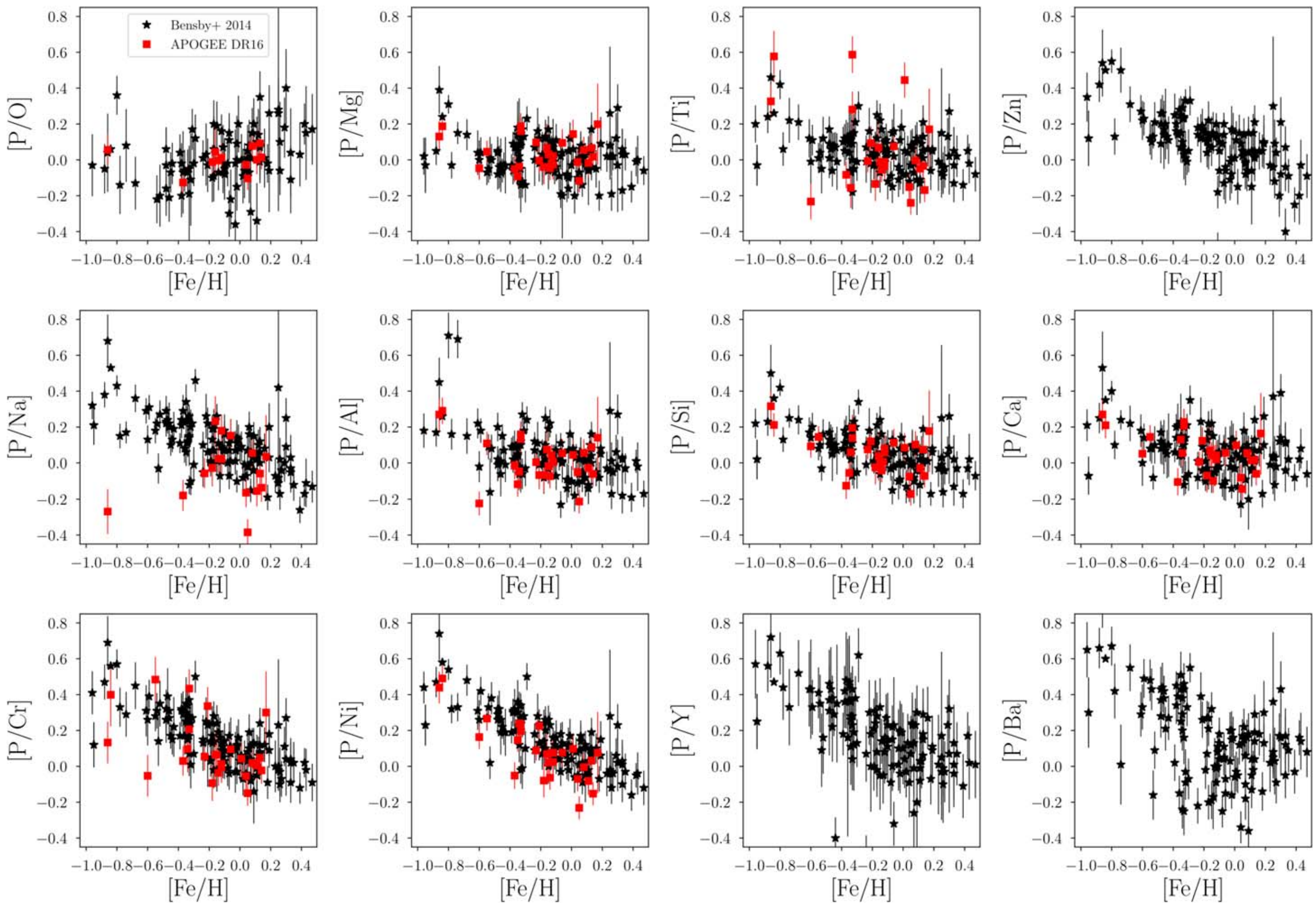

Figure 9. [P/X] vs. [Fe/H] ratios are plotted using P abundances from this work, and other abundances from Bensby et al. (2014; as black circles) and APOGEE DR16 (red squares).

4.5. Molar Phosphorus Ratios

P is a critical element for multiple biological reactions. To better connect astronomical studies of P abundances to other disciplines, Hinkel et al. (2020) analyzed stellar abundances as molar ratios. The authors then specifically compared ratios of key elements for life of C, N, Si, and P, and found the Sun has distinctive abundances compared to nearby stars (lower P/C molar ratios) and that the Earth is relatively enriched with phosphorus. The low refractory-to-volatile element ratios are consistent with other studies that compared the solar composition to solar twins (Bedell et al. 2018). We extend that analysis and have examined P relative to other key elements for life by computing the molar ratios of P/C and N/C for our stars.

We obtained C and N abundance ratios from the Hypatia Catalog (Hinkel et al. 2014) for selected stars in our sample. We chose stars that had $\log(g) > 3.5$ dex, to avoid giants that may have surface abundances affected by the first dredge-up (additional N or removed ^{12}C). In total, 46 dwarfs in our sample had both literature N and C abundances listed in the Hypatia Catalog. We used the mean abundance if stars had multiple C or N measurements, and we adopted the standard deviation from multiple abundance measurements as the abundance uncertainty. The abundances are adopted directly from the Hypatia Catalog and have not been corrected for any difference in atmospheric parameters. Molar ratios are then calculated using Equation (2) from Hinkel et al. (2020) and are plotted in Figure 10 for our sample. We have also added the stars with previously measured C, N, and P abundances (P abundances from Caffau et al. 2011, 2016; Maas et al. 2017; Caffau et al. 2019; Maas et al. 2019) from the Hypatia Catalog and previously analyzed in Hinkel et al. (2020), to compare with our additional sample.

Our results are largely consistent with the molar ratios shown in Hinkel et al. (2020). We also calculated the solar N/C and P/C ratios using abundances from Lodders et al. (2009), and we find the P/C ratio of the Sun is offset from other field stars—likely due to a slight C enrichment relative to other stars in the solar neighborhood (Bedell et al. 2018). The 46 stars with molar ratios include four stars with $[\mathrm{Fe/H}] < -0.8$; all other stars are between $-0.45 < [\mathrm{Fe/H}] < 0.47$. The four relatively metal-poor stars include the two outliers at N/C ∼0.6, HIP 38625 and HIP 17147. The two other metal-poor stars, namely the halo star HIP 100792 and the thick disk star HIP 104659, are more consistent with the rest of the sample and have respective N/C values of 0.28 and 0.20.

A combination of intrinsic abundance scatter, systematic uncertainties in atmospheric parameter derivation between different abundance studies, uncertainties in the molar ratios, and chemical evolution of more metal-poor stars may be creating the large observed scatter in the molar ratios. Additional P abundances are critical to understand the P/C evolution with [Fe/H] and to understand the range of important

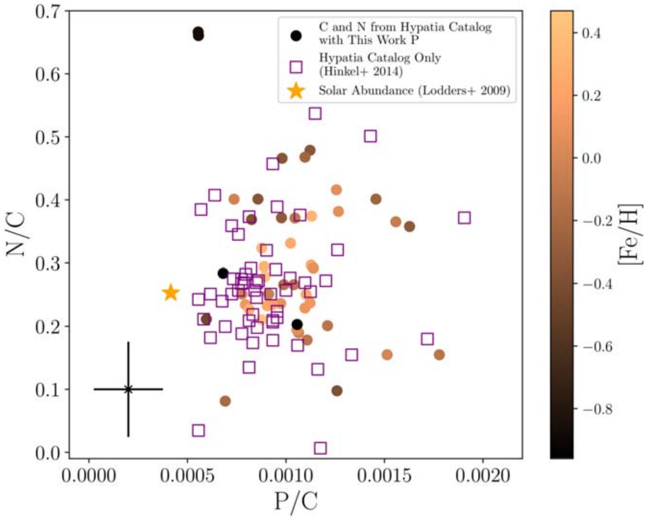

Figure 10. Molar N/C ratios compared to P/C ratios. The orange star is the solar abundance from Lodders et al. (2009). All stars in the plot have C and N abundances adopted from the Hypatia Catalog (Hinkel et al. 2014). Stars with P abundances measured in this work are shown as circles, and a color bar denotes the [Fe/H]. Literature P abundances from Hypatia are plotted as open-faced purple squares. A representative error bar is also shown in the bottom left corner.

elements for life in nearby stars. A significant variation of C/P and N/C ratios may impact life, as P may be strongly partitioned in planetary cores (Stewart & Schmidt 2007). Continuing to characterize the variations of elements, such as P, is the first step to constraining what bio-essential elements may be available in other exoplanets (Hinkel et al. 2020).

5. Conclusions

While P is an important element for life and is potentially made in multiple nucleosynthesis sites, few stellar abundances exist to test theories of P production. We measured P abundances in 163 stars using observations obtained with HPF on the HET. Our sample was selected from the previous abundance studies of Bensby et al. (2014) and APOGEE DR16 (Jönsson et al. 2020). High-S/N observations were obtained for stars that ranged over $-1.09 < [\mathrm{Fe/H}] < 0.47$. Atmospheric parameters were derived using `MINESweeper` and a combination of optical and infrared photometry, Gaia parallaxes, and Fe I equivalent widths. We derived P abundances by fitting a grid of synthetic spectra, created using MOOG (Sneden 1973) with MARCS model atmospheres (Gustafsson et al. 2008), to the P I feature at 10529.52 Å. We summarize the main conclusions of our analysis below:

1. We demonstrated the P I line at 10529.52 Å gave consistent abundances for both red giants and FGK dwarf stars. We find that our P abundances are generally consistent with previous works; however, there was significant scatter when comparing 12 stars in common with APOGEE DR16, consistent with P being relatively uncertain in APOGEE (Jönsson et al. 2020).
2. This sample of P abundances supports the results of Maas et al. (2019) that chemical evolution models do not fit the observed abundances of stars in the solar neighborhood. The best-fitting model from Cescutti et al. (2012) uses P massive star yields that have been enhanced by a factor of 2.75. However, the model does not fit the most metal-poor stars in our sample. Yield enhancements from C-O shell ingestion in massive stars may be a promising way to resolve discrepancies between models and abundances (Ritter et al. 2018).
3. We identify members of the Milky Way thin and thick disk using UVW velocities and membership criteria from Ramírez et al. (2013). We find a [P/Fe] difference of ∼0.1 dex between thin and thick disk stars, providing additional evidence that phosphorus is primarily made in CCSNe.
4. Comparisons of phosphorus to multiple difference elements in Figure 9. We find phosphorus evolves similarly to Mg and [P/X] ratios, with iron-peak or s-process elements decreasing with increasing [Fe/H]. The behavior of [P/Mg] compared to [P/Y] and [P/Ni, Cr] suggests P is primarily made in CCSNe and not in time-delayed processes for disk stars.
5. We computed molar P/C and N/C fractions for a subsample of 46 dwarf stars. We found that the solar P/C ratio is offset relative to field stars, agreeing with measurements of Hinkel et al. (2014, 2020). We also find a large scatter in the observations that may be due to different star-to-star intrinsic abundances and differences in atmospheric parameter measurement methodology in the dwarf star sample.
6. We find one star, HIP 100792, is relatively deficient in P compared to stars at similar metallicities. HIP 100792 is also a likely halo star and member of the GSE system, based on kinematics and chemistry. Further observations of low-α halo stars are needed to confirm that HIP 100792 is not an anomaly.
7. Our analysis of 163 stars overall suggests P is primarily produced in CCSNe and has evolved in lockstep with other α-elements.

The research shown here acknowledges use of the Hypatia Catalog Database, an online compilation of stellar abundance data as described in Hinkel et al. (2014, AJ, 148, 54), which was supported by NASA's Nexus for Exoplanet System Science (NExSS) research coordination network and the Vanderbilt Initiative in Data-Intensive Astrophysics (VIDA). This research has made use of the NASA Astrophysics Data System Bibliographic Services, and this research has made use of the SIMBAD database, operated at CDS, Strasbourg, France. This publication makes use of data products from the Two Micron All Sky Survey, which is a joint project of the University of Massachusetts and the Infrared Processing and Analysis Center/California Institute of Technology, funded by the National Aeronautics and Space Administration and the National Science Foundation. This publication makes use of data products from the Wide-field Infrared Survey Explorer, which is a joint project of the University of California, Los Angeles, and the Jet Propulsion Laboratory/California Institute of Technology, funded by the National Aeronautics and Space Administration. This work has made use of data from the European Space Agency (ESA) mission Gaia (https://www.cosmos.esa.int/gaia), processed by the Gaia Data Processing and Analysis Consortium (DPAC,https://www.cosmos.esa.int/web/gaia/dpac/consortium). Funding for the DPAC has been provided by national institutions, in particular the institutions participating in the Gaia Multilateral Agreement. The Hobby–Eberly Telescope (HET) is a joint project of the

University of Texas at Austin, the Pennsylvania State University, Ludwig-Maximilians-Universität München, and Georg-August-Universität Göttingen. The HET is named in honor of its principal benefactors, William P. Hobby and Robert E. Eberly. These results are based on observations obtained with the Habitable-zone Planet Finder Spectrograph on the HET. The HPF team was supported by NSF grants AST-1006676, AST-1126413, AST-1310885, AST-1517592, AST-1310875, AST-1910954, AST-1907622, AST-1909506, ATI 2009889, and ATI-2009982, and the NASA Astrobiology Institute (NNA09-DA76A) in the pursuit of precision radial velocities in the NIR. The HPF team was also supported by the Heising-Simons Foundation via grant 2017-0494. We thank the referee Dr. P. Bonifacio for suggested improvements to the manuscript. Z.G.M and N.R.H. are partially supported by a NASA ROSES-2020 Exoplanet Research Program Grant (20-XRP20 2-0125). K.H. acknowledges support from the National Science Foundation grant AST-1907417 and AST-2108736. K.H. is partly support from the Wootton Center for Astrophysical Plasma Properties funded under the United States Department of Energy collaborative agreement DE-NA0003843. This work was performed in part at the Simons Foundation Flatiron Institute's Center for Computational Astrophysics during K.H.'s tenure as an IDEA Fellow.

Software: MOOG (v2019; Sneden 1973), `scipy` (Virtanen et al. 2020), `numpy` (van der Walt et al. 2011), `matplotlib` (Hunter 2007), `astropy` (Astropy Collaboration et al. 2013), `galpy` (Bovy 2015), `emcee` (Foreman-Mackey et al. 2013), `pyia` (Price-Whelan 2018), `dustmaps` (Green et al. 2019), `MINESweeper` (Cargile et al. 2020), `iSpec` (Blanco-Cuaresma et al. 2014; Blanco-Cuaresma 2019), `ThePayne` (Ting et al. 2019), Goldilocks HPF Pipeline (Zeimann 2021).

ORCID iDs

Zachary G. Maas https://orcid.org/0000-0002-0475-3662
Keith Hawkins https://orcid.org/0000-0002-1423-2174
Natalie R. Hinkel https://orcid.org/0000-0003-0595-5132
Phillip Cargile https://orcid.org/0000-0002-1617-8917
Steven Janowiecki https://orcid.org/0000-0001-9165-8905
Tyler Nelson https://orcid.org/0000-0003-3707-5746

References

Afşar, M., Sneden, C., Wood, M. P., et al. 2018, ApJ, 865, 44
Andrews, B. H., Weinberg, D. H., Schönrich, R., & Johnson, J. A. 2017, ApJ, 835, 224
Asplund, M., Grevesse, N., Sauval, A. J., & Scott, P. 2009, ARA&A, 47, 481
Astropy Collaboration, Robitaille, T. P., Tollerud, E. J., et al. 2013, A&A, 558, A33
Bedell, M., Bean, J. L., Meléndez, J., et al. 2018, ApJ, 865, 68
Belokurov, V., Erkal, D., Evans, N. W., Koposov, S. E., & Deason, A. J. 2018, MNRAS, 478, 611
Bensby, T., Feltzing, S., & Oey, M. S. 2014, A&A, 562, A71
Berzinsh, U., Svanberg, S., & Biemont, E. 1997, A&A, 326, 412
Binney, J. 2012, MNRAS, 426, 1324
Blanco-Cuaresma, S. 2019, MNRAS, 486, 2075
Blanco-Cuaresma, S., Soubiran, C., Heiter, U., & Jofré, P. 2014, A&A, 569, A111
Böcek Topcu, G., Afşar, M., Sneden, C., et al. 2019, MNRAS, 485, 4625
Bonifacio, P., Monaco, L., Salvadori, S., et al. 2021, A&A, 651, A79
Bovy, J. 2015, ApJS, 216, 29
Buder, S., Lind, K., Ness, M. K., et al. 2022, MNRAS, 510, 2407
Caffau, E., Andrievsky, S., Korotin, S., et al. 2016, A&A, 585, A16
Caffau, E., Bonifacio, P., Faraggiana, R., & Steffen, M. 2011, A&A, 532, A98
Caffau, E., Steffen, M., Sbordone, L., Ludwig, H. G., & Bonifacio, P. 2007, A&A, 473, L9
Caffau, E., Bonifacio, P., Oliva, E., et al. 2019, A&A, 622, A68
Cargile, P. A., Conroy, C., Johnson, B. D., et al. 2020, ApJ, 900, 28
Casagrande, L., Schönrich, R., Asplund, M., et al. 2011, A&A, 530, A138
Cescutti, G., Matteucci, F., Caffau, E., & François, P. 2012, A&A, 540, A33
Choi, J., Dotter, A., Conroy, C., et al. 2016, ApJ, 823, 102
Conroy, C., Bonaca, A., Cargile, P., et al. 2019, ApJ, 883, 107
Das, P., Hawkins, K., & Jofré, P. 2020, MNRAS, 493, 5195
Edvardsson, B., Andersen, J., Gustafsson, B., et al. 1993, A&A, 275, 101
ESA Special Publication 1997, EP-1200, The Hipparcos and Tycho Catalogues (Noordwijk: ESA)
Feltzing, S., Fohlman, M., & Bensby, T. 2007, A&A, 467, 665
Feuillet, D. K., Sahlholdt, C. L., Feltzing, S., & Casagrande, L. 2021, MNRAS, 508, 1489
Foreman-Mackey, D., Hogg, D. W., Lang, D., & Goodman, J. 2013, PASP, 125, 306
Franchini, M., Morossi, C., Di Marcantonio, P., et al. 2020, ApJ, 888, 55
Fuhrmann, K. 1998, A&A, 338, 161
Fukue, K., Matsunaga, N., Kondo, S., et al. 2021, ApJ, 913, 62
Gaia Collaboration, Prusti, T., de Bruijne, J. H. J., et al. 2016, A&A, 595, A1
Collaboration, Gaia, Brown, A. G. A., Vallenari, A., et al. 2021, A&A, 649, A1
Gray, D. F., Tycner, C., & Brown, K. 2000, PASP, 112, 328
Green, G. M., Schlafly, E., Zucker, C., Speagle, J. S., & Finkbeiner, D. 2019, ApJ, 887, 93
Grevesse, N., Asplund, M., & Sauval, A. J. 2007, SSRv, 130, 105
Gustafsson, B., Edvardsson, B., Eriksson, K., et al. 2008, A&A, 486, 951
Hawkins, K., Jofré, P., Masseron, T., & Gilmore, G. 2015, MNRAS, 453, 758
Hawkins, K., Masseron, T., Jofré, P., et al. 2016, A&A, 594, A43
Hayden, M. R., Bovy, J., Holtzman, J. A., et al. 2015, ApJ, 808, 132
Haywood, M., Di Matteo, P., Lehnert, M. D., et al. 2018, ApJ, 863, 113
Heiter, U., Lind, K., Bergemann, M., et al. 2021, A&A, 645, A106
Helmi, A., Babusiaux, C., Koppelman, H. H., et al. 2018, Natur, 563, 85
Hinkel, N. R., Hartnett, H. E., & Young, P. A. 2020, ApJL, 900, L38
Hinkel, N. R., Timmes, F. X., Young, P. A., Pagano, M. D., & Turnbull, M. C. 2014, AJ, 148, 54
Høg, E., Fabricius, C., Makarov, V. V., et al. 2000, A&A, 355, L27
Holmberg, J., Nordström, B., & Andersen, J. 2007, A&A, 475, 519
Holtzman, J. A., Hasselquist, S., Shetrone, M., et al. 2018, AJ, 156, 125
Hunter, J. D. 2007, CSE, 9, 90
Jacobson, H. R., Thanathibodee, T., Frebel, A., et al. 2014, ApJL, 796, L24
Jönsson, H., Allende Prieto, C., Holtzman, J. A., et al. 2018, AJ, 156, 126
Jönsson, H., Holtzman, J. A., Allende Prieto, C., et al. 2020, AJ, 160, 120
Kobayashi, C., Karakas, A. I., & Umeda, H. 2011, MNRAS, 414, 3231
Kobayashi, C., Umeda, H., Nomoto, K., Tominaga, N., & Ohkubo, T. 2006, ApJ, 653, 1145
Kondo, S., Fukue, K., Matsunaga, N., et al. 2019, ApJ, 875, 129
Koo, B.-C., Lee, Y.-H., Moon, D.-S., Yoon, S.-C., & Raymond, J. C. 2013, Sci, 342, 1346
Kurucz, R. L. 1979, ApJS, 40, 1
Kurucz, R. L. 2013, ATLAS12: Opacity sampling model atmosphere program, Astrophysics Source Code Library, ascl:1303.024
Lindegren, L., Bastian, U., Biermann, M., et al. 2021, A&A, 649, A4
Lockwood, G. W., Skiff, B. A., Henry, G. W., et al. 2007, ApJS, 171, 260
Lodders, K. 2021, SSRv, 217, 44
Lodders, K., Palme, H., & Gail, H. P. 2009, Solar System, Vol. 4B (Berlin: Springer), 712
Maas, Z. G., Cescutti, G., & Pilachowski, C. A. 2019, AJ, 158, 219
Maas, Z. G., Pilachowski, C. A., & Cescutti, G. 2017, ApJ, 841, 108
Mahadevan, S., Ramsey, L., Bender, C., et al. 2012, Proc. SPIE, 8446, 84461S
Mahadevan, S., Ramsey, L. W., Terrien, R., et al. 2014, Proc. SPIE, 9147, 91471G
Marchetti, T., Contigiani, O., Rossi, E. M., et al. 2018, MNRAS, 476, 4697
Masseron, T., García-Hernández, D. A., Santoveña, R., et al. 2020a, NatCo, 11, 3759
Masseron, T., García-Hernández, D. A., Zamora, O., & Manchado, A. 2020b, ApJL, 904, L1
Matsunaga, N., Taniguchi, D., Jian, M., et al. 2020, ApJS, 246, 10
Molaro, P., Levshakov, S. A., Monai, S., et al. 2008, A&A, 481, 559
Nelson, D. L., & Cox, M. M. 2017, Lehninger Principles of Biochemistry (7th edn.; Freeman: San Francisco)
Ninan, J. P., Bender, C. F., Mahadevan, S., et al. 2018, Proc. SPIE, 10709, 107092U
Nissen, P. E., & Schuster, W. J. 2010, A&A, 511, L10
Nissen, P. E., & Schuster, W. J. 2011, A&A, 530, A15
Paxton, B., Bildsten, L., Dotter, A., et al. 2011, ApJS, 192, 3
Placco, V. M., Sneden, C., Roederer, I. U., et al. 2021, RNAAS, 5, 92

Prantzos, N., Abia, C., Limongi, M., Chieffi, A., & Cristallo, S. 2018, MNRAS, 476, 3432

Price-Whelan, A. 2018, adrn/pyia: v0.2, Zenodo, doi:10.5281/zenodo.1228136

Ramírez, I., Allende Prieto, C., & Lambert, D. L. 2013, ApJ, 764, 78

Ritter, C., Andrassy, R., Côté, B., et al. 2018, MNRAS, 474, L1

Roederer, I. U., Jacobson, H. R., Thanathibodee, T., Frebel, A., & Toller, E. 2014, ApJ, 797, 69

Roederer, I. U., Placco, V. M., & Beers, T. C. 2016, ApJL, 824, L19

Sadakane, K., & Nishimura, M. 2022, PASJ, 74, 298

Schlesinger, W., & Bernhardt, E. 2013, Biogeochemistry (Boston, MA: Academic Press)

Skrutskie, M. F., Cutri, R. M., Stiening, R., et al. 2003, 2MASS All-Sky Point Source Catalog, 1.0, IRSA, doi:10.26131/IRSA2

Skrutskie, M. F., Cutri, R. M., Stiening, R., et al. 2006, AJ, 131, 1163

Sneden, C. 1973, ApJ, 184, 839

Sneden, C., Afşar, M., Bozkurt, Z., et al. 2021, AJ, 161, 128

Soubiran, C., Le Campion, J.-F., Brouillet, N., & Chemin, L. 2016, A&A, 591, A118

Speagle, J. S. 2020, MNRAS, 493, 3132

Spite, M., Peterson, R. C., Gallagher, A. J., Barbuy, B., & Spite, F. 2017, A&A, 600, A26

Stewart, A. J., & Schmidt, M. W. 2007, GeoRL, 34, L13201

Thiabaud, A., Marboeuf, U., Alibert, Y., Leya, I., & Mezger, K. 2015, A&A, 580, A30

Ting, Y.-S., Conroy, C., Rix, H.-W., & Cargile, P. 2019, ApJ, 879, 69

van der Walt, S., Colbert, S. C., & Varoquaux, G. 2011, CSE, 13, 22

Virtanen, P., Gommers, R., Oliphant, T. E., et al. 2020, NatMe, 17, 261

Weinberg, D. H., Holtzman, J. A., Hasselquist, S., et al. 2019, ApJ, 874, 102

Woosley, S. E., & Weaver, T. A. 1995, ApJS, 101, 181

Wright, E. L., Eisenhardt, P. R. M., Mainzer, A. K., et al. 2010, AJ, 140, 1868

Wright, E. L., Eisenhardt, P. R. M., Mainzer, A. K., et al. 2011, AllWISE Source Catalog, 1.0, IRSA, doi:10.26131/IRSA1

Yuan, Z., Myeong, G. C., Beers, T. C., et al. 2020, ApJ, 891, 39

Zeimann, G. 2021, Goldilocks: Habitable Planet Finder (HPF) Automatic Reduction Software, Commit: fda0b45, GitHub, https://github.com/grzeimann/Goldilocks_Documentation